ARTICLE

A facile route to plastic inorganic electrolytes for all-solid state batteries based on molecular design

Insang You[a], Baltej Singh[a], Mengyang Cui[b], Gillian Goward[b], Lanting Qian[a], Zachary Arthur[c], Graham King[c] and Linda F. Nazar[a]*

Solid-state lithium batteries are on the threshold of commercialization as an alternative to liquid electrolyte batteries. Glassy or amorphous solid electrolytes could bring crucial benefits, but their lack of periodicity impedes structure-derived material design. Here, we report an approach for glassy electrolyte design based on well-defined lithium metal oxychloride linear oligomers. By packing these oligomers formed by oxygen-bridged chloroaluminates, a glassy solid model is constructed. Li ions in mixed-anion coordination with distorted polyhedra favor good lithium conductivity (1.3 mS.cm^{-1} at 30 °C). The frustrated Li-ion geometry and non-crystallinity promote conformational dynamics of the oligomer backbone that generates mechanical plasticity. Ab-initio molecular dynamics simulations depict the conformational motion that resembles that of organic molecules. Our all-solid-state battery based on this solid electrolyte shows exceptional long term electrochemical stability with a high-nickel NCM cathode. This work shows the impact of targeted structure models for rational design of glassy plastic electrolytes.

Introduction

Lithium-ion batteries for electric vehicles and energy storage systems are an indispensable part of a clean-energy future, and included in these is the prospect of all-solid-state designs. The demand for high performance solid-state electrolytes (SSEs), which are an essential component of such devices, has drawn much attention owing to their non-flammability and mechanical toughness[1] which potentially allow the use of an Li metal anode.[2] Fundamental research in SSEs has revealed many mechanisms of superionic conductivity based on mixed-polyanions,[3,4] geometrical frustration,[5,6] concerted ion migration,[7] high-entropy systems,[8] ion site percolation[9] and phonon-ion interactions.[10] Nonetheless, the mechanical properties of hard materials present a practical challenge in the context of SSE's commercialization.[11] Since crystalline ceramics do not permit structural re-arrangement below their melting point, there is inherent interface resistance between solid particles.[12] This required fundamental studies based on atomic scale investigations;[13] meanwhile, suppressing the crystallinity – moving towards amorphous materials – has been suggested as a promising solution.[14] While there is vast opportunity in creating disordered structures, typical synthesis methods like mechanochemistry can be challenging to scale up to a manufacturing level.[15]

Recently, some glassy SSEs, despite being comprised of hard anions, have demonstrated fascinating clay-like mechanical properties and an accompanying low glass transition temperature (T_g) below room temperature. These are exemplified by gallium fluorochloride polyanion-based materials that exhibit high conductivity for Li$^+$-ions[16] and Mg^{2+}-ions.[17] The mechanism of enhanced ion dynamics was rationalized by charge clustering[18] and also interestingly, by the formation of shear-transformation-zones.[19] More recently, an aluminium oxychloride-based viscoelastic electrolyte was reported,[20] which is a promising candidate as an SSE because of the low cost and abundance of aluminum.[21,22] Proposed structures for the glassy materials were obtained from *ab-initio* molecular dynamics (AIMD) melt-quench protocols and *ab-initio* density functional theory (DFT). While these have provided much invaluable insight, the accuracy of a simulated glass structure is intrinsically limited due to artificial periodic boundary conditions. Furthermore, in practice, *ab-initio* simulations cannot explore all the possible configurations in a glass within the restricted timeframe offered by most computational resources. Since ion dynamics are dictated by structure, starting off with a realistic model is crucial for understanding the behaviour of glassy-state electrolytes.

Here, we demonstrate the simple, cost-effective synthesis of a new glassy lithium aluminium oxychloride (LAOC) plastic electrolyte generated by a straightforward method, and different from previously reported.[20,21] We targeted a mixture of linear anionic oligomers as the building blocks that constitute the major component. One is the $Li_3Al_3O_2Cl_8$ trimer, whose M-O-Cl framework we propose is isostructural with crystalline $Si_3O_2Cl_8$,[23] but where (Al^{3+} + Li^+) replaces Si^{4+}. That aliovalent substitution is well established in solid state ionics.[24] Two other linear trimers can form by releasing LiCl from $Li_3Al_3O_2Cl_8$, which are stabilized by chlorine bridges across the Al: namely $Li_2Al_3O_2Cl_7$ and $LiAl_3O_2Cl_6$. The latter has been reported, and our mass spectrometry studies confirm the trimeric nature of the oligomers, as discussed below. Our LAOC solid model comprises the packing of these oligomers, whose physicochemical properties (i.e. conductivity, plasticity, etc) can be generalized from

the local structure despite the lack of crystalline periodicity. Unlike a typical inorganic glass, the nature of LAOC resembles an amorphous organic solid, whose anionic oligomer entities constitute strong bonds (Al-Cl and Al-O) while the oligomers form a solid through relatively weak bonding (Li-Cl and Li-O). The weakly bonded network enables significant Li and Cl dynamics that cannot be portrayed by a conventional amorphous structure model made up of an arbitrary distribution of elements.

In this model, we define two types of ion dynamics. First, Li-migration is enhanced by the large geometrical frustration of the Li-ion environment, promoted by mixed coordination of Cl and O anions. The existence of $Li[O_xCl_y]$ coordination is suggested by ^7Li solid-state nuclear magnetic resonance (ssNMR) spectroscopy, and the nature of Li-O bonding as a dative bond is confirmed through X-ray absorption spectroscopy (XAS). Second, rotational motion of the terminal Cl groups is observed even at 300 K based on AIMD simulations. The motion arises from the conformational dynamics of the oligomer backbone (rotational and bending motions), leading to mechanical plasticity through the creation of transient local free volume, as observed in organic polymers. The rotational motion is clearly distinguished from vibrational motion by its low frequency response (GHz-THz). The analytical method is borrowed from the conformational study of polymeric materials and applied to inorganic glasses for the first time. Since LAOC is composed of "hard" anions (O and Cl), it shows excellent electrochemical stability (above 4.3 V vs Li$^+$/Li) along with plasticity, which is a unique advantage for all-solid-state-batteries (ASSBs) as we demonstrate with full cells.

Results and discussion

Oligomer-based SSE and local structure investigation

The previous reports on lithium aluminium oxychlorides utilized a solid-state reaction of LiCl, $AlCl_3$ and Sb_2O_3 to incorporate oxygen into $LiAlCl_4$, described as $4LiAlCl_4 + Sb_2O_3 \rightarrow 4LiAlCl_{2.5}O_{0.75} + 2 SbCl_3$ (Al:O ratio of 4:3).[20] While $SbCl_3$ is sublimed above 225 °C, it is difficult to fully remove, requiring a second long heat treatment at 250 °C.[21] Our synthesis employs a simple approach utilizing $LiAlCl_4$, $AlCl_3$ and $AlCl_3·6H_2O$ as reactants (**Fig. 1b**) - at an Al/O ratio of 3:2 fixed by the reactant stoichiometry in order to target the trimers. The latter provides the oxygen to form the lithium aluminium oxychloride, and hydrogen is removed as HCl.[25] This was confirmed by the complete absence of protons in its ^1H ssNMR spectrum (**Fig. S1**). The white lithium aluminium oxychloride (LAOC) solid we obtained exhibited an ionic conductivity of 1.3 mS.cm^{-1} with an activation energy of 0.47 eV (**Fig. S2**) and low electrical conductivity on the order of 10^{-10} S/cm (**Fig. S3**). While the conductivity is comparable to other lithium aluminium oxychlorides, it is over 10^3 fold higher than crystalline $LiAlCl_4$ (*P21/c*; 10^{-3} mS/cm) and 10^2 fold higher than $LiAlCl_4$ where tetrahedral defects are induced by high-energy ball-milling.[22] Importantly, the transference number of 0.98, measured by Watanabe method,[26,27] is close to one - indicating a single-ion conductor - and much higher than the value of 0.69 reported in ref. 20, suggesting a different nature of the product (see Experimental, **Fig. S4** and **Table S1**).
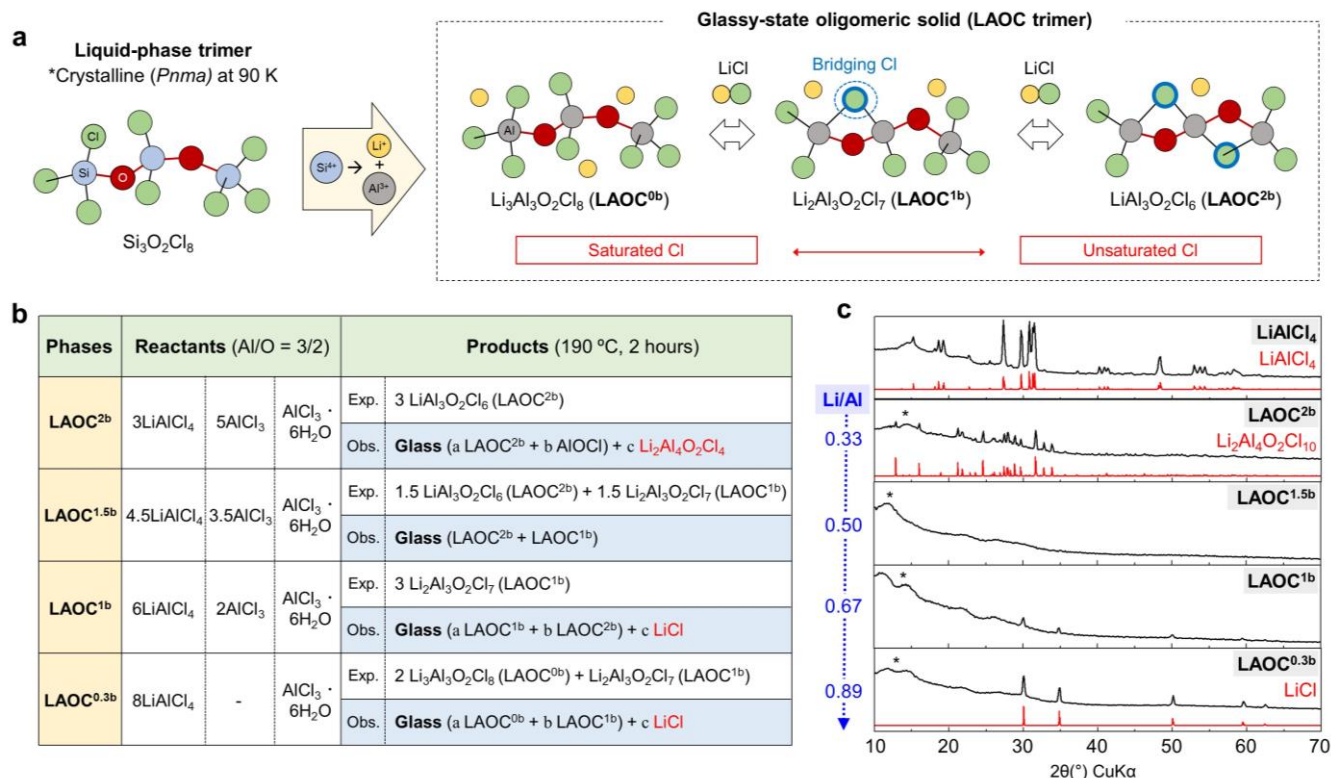

Figure 1. Structural overview of LAOC and its synthesis. (a) LAOC trimer structure inspired by $Si_3O_2Cl_8$. The superscript of LAOC^x denotes the number of bridging Cl; **(b)** Synthesis route for LAOC trimers. Except for LAOC$^{1.5b}$, there was a deviation between the expected (exp.) and observed (obs.) phases, because of the presence of LiCl or crystallized $Li_2Al_4O_2Cl_{10}$ (reference patterns in red). HCl gas is omitted in the products. **(c)** XRD patterns of synthesized LAOC according to the amount of incorporated LiCl. The simulated diffraction pattern from the reference structure is shown in red. The contribution from the Kapton film used to protect the samples from air is marked with an asterisk.

Chloroaluminates are known to be complex mixtures of oligomers in equilibrium, and identifying the precise components can be difficult. Our Al/O ratio of 3:2 was inspired by that in the known crystalline silicon trimer, $Si_3O_2Cl_8$ (**Fig. 1a**) the rationale being that Al^{3+} could replace Si^{4+} in the structure, with Li^+ providing charge balance and the carriers for Li-ion conductivity. This proposed, fully Cl-saturated oligomer - $Li_3Al_3O_2Cl_8$ - contains only terminal Cl groups ("LAOC[0b]"), and the Al-O-Al linkages allow for a flexible backbone (**Fig. 1a**). While this oligomer has the highest Li/Al ratio, release of Cl^- (+ Li^+) would form Cl-bridged species: namely $Li_2Al_3O_2Cl_7$ (LAOC[1b]) and $LiAl_3O_2Cl_6$ (LAOC[2b]; **Fig. 1a**). These would be expected to be in equilibrium, and $Al_3O_2Cl_6^-$ has been reported (in aqueous solution).[28] Indeed, their "molecular" nature is supported by the solubility of synthesized LAOC in an organic solvent that allowed us to conduct electrospray ionization (ESI) mass spectrometry analysis. We identified $Al_3O_2Cl_6^-$ in LAOC[1.5b] (i.e., a mixture of LAOC[1b] + LAOC[2b]) with the observation of m/z species of 322.8, 324.8, 326.8, 328.8 in the mass spectrum (distributed by chlorine isotopes; (**Fig. S5**). The divalent $Al_3O_2Cl_7^{2-}$ anion was not detected owing to its much lower solubility in the ESI solvent (acetonitrile) and equilibration to favor $[Al_3O_2Cl_6^- + LiCl]$, (**Fig. S6**). Other chloroaluminates suggested in previous studies (e.g. $Al_2OCl_5^-$, $Al_3OCl_8^-$)[21,25,28] were not observed.

The thermodynamic stability of LAOC depends on the degree of chloride saturation. LiCl is ex-solved in the glass at high degrees of Cl-saturation (<1.5b) as shown in the XRD patterns of LAOC[0.3b] (1/3LAOC[1b]+2/3LAOC[0b]) and LAOC[1b] (**Fig. 1c**), suggesting that the fully terminal-Cl structure is not stable at room temperature. At a low

degree of saturation (>1.5b), LAOC[2b] is a mixed phase with crystalline $Li_2Al_4O_2Cl_{10}$ (*Pbca*) present, as indicated by the appearance of sharp diffraction peaks. The material is an oligomer isostructural to $Ag_2Al_4O_2Cl_{10}$.[29] We confirmed this by Rietveld refinement against the X-ray diffraction data (**Fig. S7**, **Table S2**). On the other hand, the XRD pattern of LAOC[1.5b] reveals a purely amorphous phase (**Fig. 1c**) without any residual $Li_2Al_4O_2Cl_{10}$ as confirmed by Fourier transform infrared spectroscopy (**Fig. S8**).[30]

Support for our LAOC model was obtained from molecular dynamics simulation; periodic solids were generated by distributing the LAOC[0b] trimers to form a supercell, followed by AIMD melt-quenching at 600 K (**Fig. 2a**). For comparison, a conventional amorphous model was generated by melt-quenching the crystalline form of $LiAlCl_4$ after exchanging some of the Cl by O. The local structure of the simulated LAOC[0b] model, along with a typical example from the amorphous model are displayed in **Fig. 2b.** The backbone of the proposed oligomers ($Li_{3-x}Al_3O_2Cl_{8-x}$) is formed by Al-O bonds, and the O interacts with Li through a weak dative bond with its lone pair (**Fig. 2a**). While one local coordination environment ("LiCl₃O₂") is illustrated as an example, the Li environment is highly fluxional, and a range of environments are sampled during the simulations at 600 K (see **Fig. 3**). In the amorphous model, however, the non-bridging oxygen forms an ionic bond with Li (**Fig. 2b**).

To probe the nature of the oxygen in LAOC, we utilized oxygen *K*-edge XAS. The lack of an ionic O-Li^+ bond in LAOC compositions (0.3b and 1.5b) was confirmed by their XAS spectra (**Fig. 2c**) that exhibit a broad feature at 540 eV. This value is characteristic of Al-O-Al in a
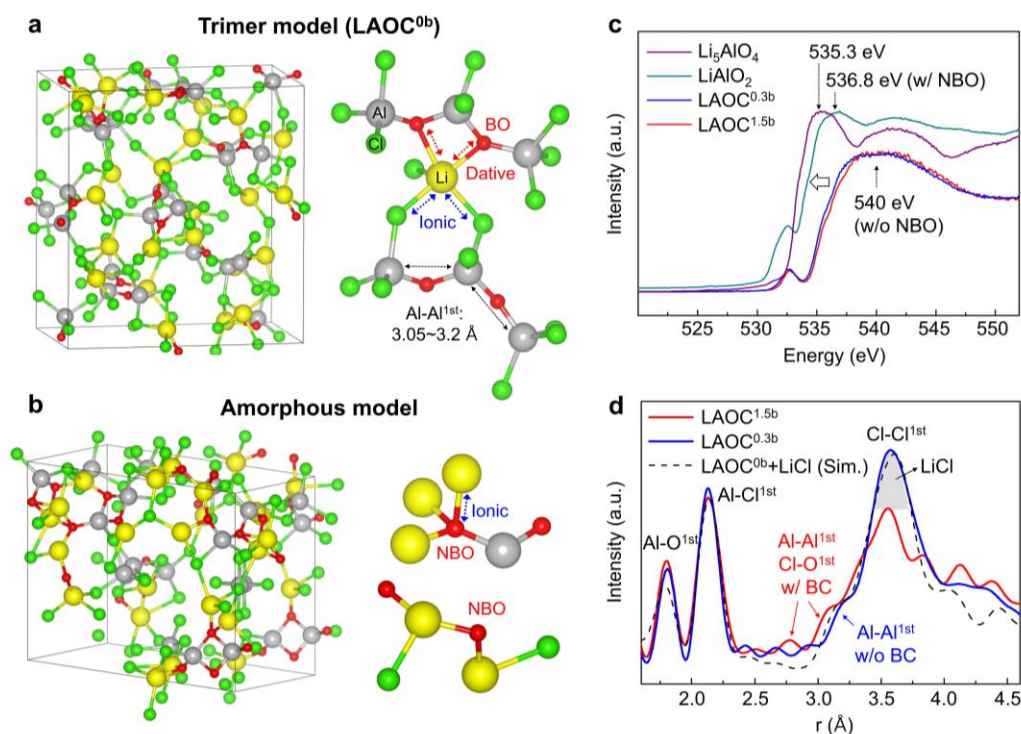

Figure 2. Local structure analysis of LAOC based on AIMD-simulated structures. (a) AIMD-simulated structure model for LAOC[0b], melt-quenched at 600 K. The supercell has 8 LAOC[0b] trimers. The local structure example (two trimers with one Li) was taken from the supercell. **(b)** Amorphous structure model based on melt-quenched (600 K) AIMD simulation. Characteristic local structures were taken from the model, where NBO indicates non-bridging oxygen. **(c)** Observed oxygen *K-edge* XAS of LAOC and lithium aluminate where the edge shows the existence of NBO. **(d)** Observed PDF of LAOC[1.5b] and LAOC[0.3b]; the simulated PDF for LAOC[0.3b] is compared to the simulated LAOC[0b] structure with the addition of LiCl. BC stands for bridging Cl.

covalent environment such as Al_2O_3.[31] In alkali aluminium oxides such $LiAlO_2$ and Li_5AlO_4 where oxygen is also polarized by bonding to Li^+ (i.e., as LiO_4 moieties), the edge shifts to much lower energy: 536.8 eV and 535.3 eV respectively.[32,33]

The synchrotron X-ray pair distribution function (PDF) data for LAOC[1.5b] and LAOC[0.3b] are shown in **Fig. 2d** and compared with that obtained from AIMD simulation for LAOC[0b]. The characteristic Al-O and Al-Cl distances in the first shell are the same. However, we observe shorter Al-Al[1st] and Cl-O[1st] distances (2.7~3.0 Å) for LAOC[1.5b] compared to LAOC[0.3b] (3.05~3.2 Å), which we ascribe to the bridging Cl in the two proposed trimers that shortens the Al-Al[1st] distance (**Fig. S9**). The experimental PDF for LAOC[0.3b] agrees quite well with the PDF generated for simulated LAOC[0b] when ~10% LiCl is added (LAOC[0b]:LiCl = 88:12, R_w=0.248). Hence, based on the local structure analysis, we propose that LAOC is constructed primarily from anionic aluminum oxychloride trimers, weakly bound by Li cations. We also simulated extended chain models, particularly the tetramer ($Li_4Al_4O_3Cl_{10}$), but the energy above hull increased significantly (365.9 meV/atom) and is much higher than the LAOC[0b] model (61 meV/atom) (**Fig. S10**). The E_{hull} of LAOC[0b] is below 67 meV/atom which represents a criterion for synthesizable metastable materials,[34] but that of the tetramer means it is too high to be realized at room temperature, even when compared to the extended criterion of 200 meV/atom.[35] Indeed, although polymeric aluminium oxy(sulfo)chlorides were synthesized based on $KAlOCl_2$[36] and $CsAlSCl_2$,[37] these were reported only at high temperature.

Coordination environments of Li observed by solid-state NMR

The Li-ion coordination in LAOC was probed by ^7Li magic angle spinning (MAS) ssNMR spectroscopy at 850 MHz (**Fig. 3a**). As the chemical shift is mainly determined by the first-anion shell, crystalline materials ($LiAlCl_4$ and $Li_2Al_4O_2Cl_{10}$) were used as references. In the ssNMR of glassy LAOC[1.5b], three resonances (1 - 3) were observed (**Fig. 3a**). Based on the well-established semi-empirical correlation between the lithium coordination number/environment and chemical shift,[38,39] we assign these to 6, 5 and 4 coordinate Li in order of increasing frequency. Specifically, at the lowest frequency, Peak 3 (-1.05 ppm) is assigned to Li in a 6-coordinate $Li[Cl_6]$ environment, owing to the similarity in the chemical shift with $LiAlCl_4$ which exhibits octahedral Li-coordination (**Fig. 3b**). We confirmed that this resonance in LAOC is *not* due to residual LiCl by VT-ssNMR, nor from $LiAlCl_4$ as determined by Raman spectroscopy (see **Fig. S11** for details). Compared to the 5-coordinate $Li[Cl_5]$ environment in $Li_2Al_4O_2Cl_{10}$ at -0.8 ppm, Peak 2 (-0.55 ppm) is shifted to slightly higher frequency, strongly suggesting that these resonances originate from mixed 5-coordination by both Cl and O ($Li[O_nCl_{5-n}]$, 0<n<5). The higher electronegativity of O compared to Cl is predicted to induce a small increase in chemical shift due to deshielding.[40] Lastly, Peak 1 (0.05 ppm) is assigned to 4-coordinate ($Li[O_mCl_{4-m}]$, 0≤m<4) species. We note that because LAOC[1.5b] is likely a mixture of two trimers, possibly with different Li-ion coordination, it is not possible to assign the resonances more precisely. These data are compared with the Li geometries extracted from the AIMD-simulated LAOC in **Fig. 3c**. Due to the artificial periodic boundary condition introduced during AIMD-simulations and the existence of a weakly bonded network, the Li-ion polyhedra are only intended to
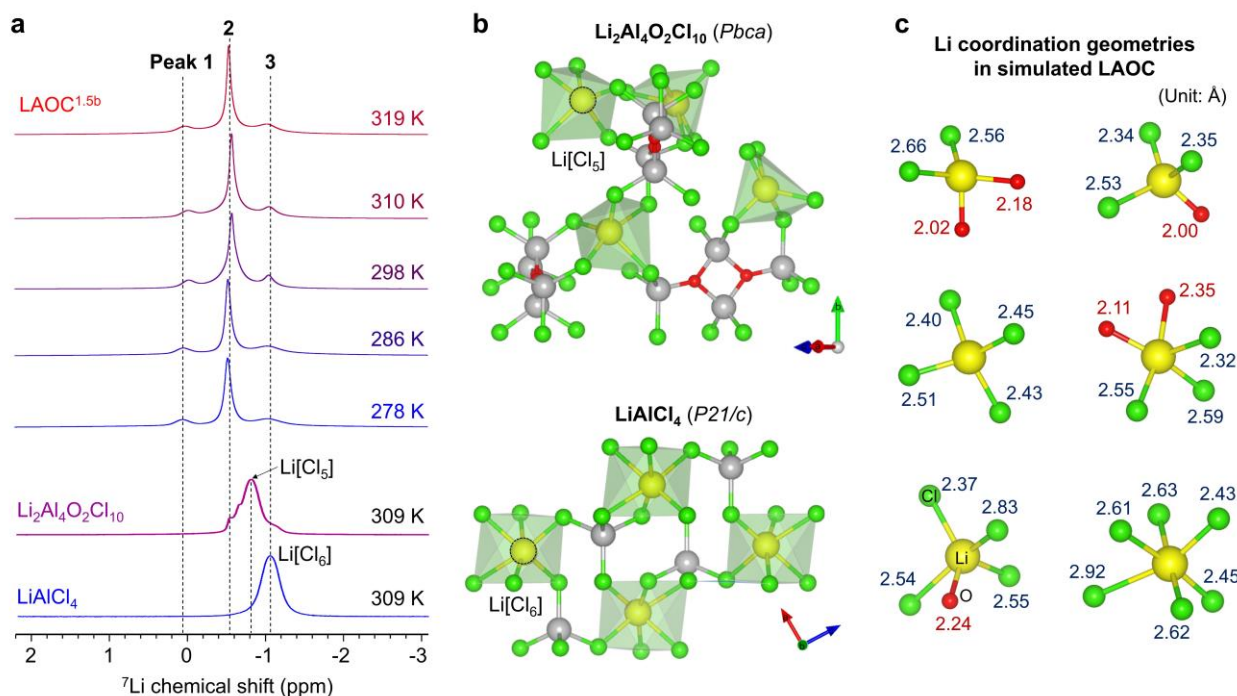

Figure 3. Li coordination environment in LAOC. (a) ^7Li MAS ssNMR spectra recorded for LAOC[1.5b] at various temperatures (VT). $LiAlCl_4$ and $Li_2Al_4O_2Cl_{10}$ serve as references. Anions in the square bracket denote the coordination environment of the Li site. **(b)** Crystal structures of $Li_2Al_4O_2Cl_{10}$ (top) and $LiAlCl_4$ (bottom). **(c)** 4-, 5- and 6-coordinate Li environments in the AIMD-simulated LAOC structure model. Bond lengths between Li and the corresponding anions are labelled.

ARTICLE

reveal feasible coordination geometries, not to identify them. Nonetheless, the results are in good accord with the ^{7}Li NMR findings. The Li[Cl$_6$] moiety, Li[O$_n$Cl$_{5-n}$] and Li[O$_m$Cl$_{4-m}$] moieties represent environments assigned to Peaks 3 -1. Multiple Li[O$_m$Cl$_{4-m}$] motifs may contribute to Peak 1 given its breadth, while its chemical shift (*vis a vis* Li[Cl$_6$]) is the same as reported for Li[Cl$_4$] defects generated in ball-milled LiAlCl$_4$.[41]

All the peaks in LAOC$^{1.5b}$ exhibit motional narrowing in the NMR spectra, but upon increasing the temperature, the normalized integrated intensity of the Peak 2 rises from 0.5 to 0.75, while the combined intensity of Peaks 1 and 3 decreases from 0.5 to 0.25 (**Fig. S12**). The population shift with temperature change reflects their relative energy depth between the Li coordination sites as observed previously in both crystalline oxide SSEs[42] and clay-like glassy SSEs.[18] The increasing thermal population of Peak 2 indicates that the Li ions in the [O$_n$Cl$_{5-n}$] coordination site are in a higher energy state than the others. This is consistent with the smaller T$_1$ relaxation time of Peak 2 (2.1 s) compared to Peak 1 (5.7 s) and 3 (3.7 s) (**Fig. S13**). The raised energy state of Li[O$_n$Cl$_{5-n}$] could originate from the accelerated geometrical frustration by low polyhedron symmetry (5-coordination) and also bonding length asymmetry (Li-O: 2.0~2.3 Å, Li-Cl: 2.3~2.6 Å) (**Fig. 3c**), while a long Li-Cl distance (~2.9 Å) was observed occasionally in the simulations. We also carried out ^{27}Al MAS ssNMR. While two major peaks (103 ppm, 80 ppm) were observed in LAOC$^{1.5b}$, distinguishable from tetrahedral Al in LiAlCl$_4$ (*P21/c*; 98 ppm), extensive peak broadening owing to the strong quadrupolar effect of ^{27}Al precluded a more detailed analysis.

Understanding ion dynamics through AIMD simulation

The identification of a plausible structural model allows us to simulate ion dynamics in glassy LAOC. During AIMD simulations, the "saturated" LAOC^{0b} (Li$_3$Al$_3$O$_2$Cl$_8$) remained stable between 300 and 700 K. At 800 K, it polymerized through the formation of Al-O-Al bonds (**Fig. S14a**), consistent with the decomposition temperature observed by thermogravimetric analysis (TGA) (**Fig. S15**). In contrast, the LAOC^{1b} (Li$_2$Al$_3$O$_2$Cl$_7$) oligomer formed additional Al-Cl-Al bonds even at 300 K, facilitated through its "unsaturated" component (**Fig. S14b**). Thus, we utilized the LAOC^{0b} model to examine the behaviour of discrete oligomers during AIMD simulation at various temperatures.

Fig. 4a (top) presents the mean squared displacement (MSD) for Li and Cl, showing notable displacement for both at 400 K. At 600 K (**Fig. 4a**, bottom), the MSD of Li increased substantially compared to Cl. Analysis of the MSD data collected between 400 and 700 K provides a diffusion constant from which the Li-ion conductivity can be calculated via the Nernst-Einstein relation; extrapolation to 300 K yields a value of σ$_i$ ~2.8 mS/cm (**Fig. S16**). This is in good accord with the experimental value of 1.2 mS/cm, indicating that the trimer-based model effectively demonstrates the ion dynamics of the glassy structure. The Li isosurface density in **Fig. 4b** shows the 3D migration path between the trimers. Similarly, Cl also shows prominent isosurfaces in **Fig. 4c** but bound to the trimer. Intriguingly, many isosurfaces of Cl display a circular shape.

To ascertain whether the circular isosurface of Cl arises from rotational motion rather than vibration, we conducted an
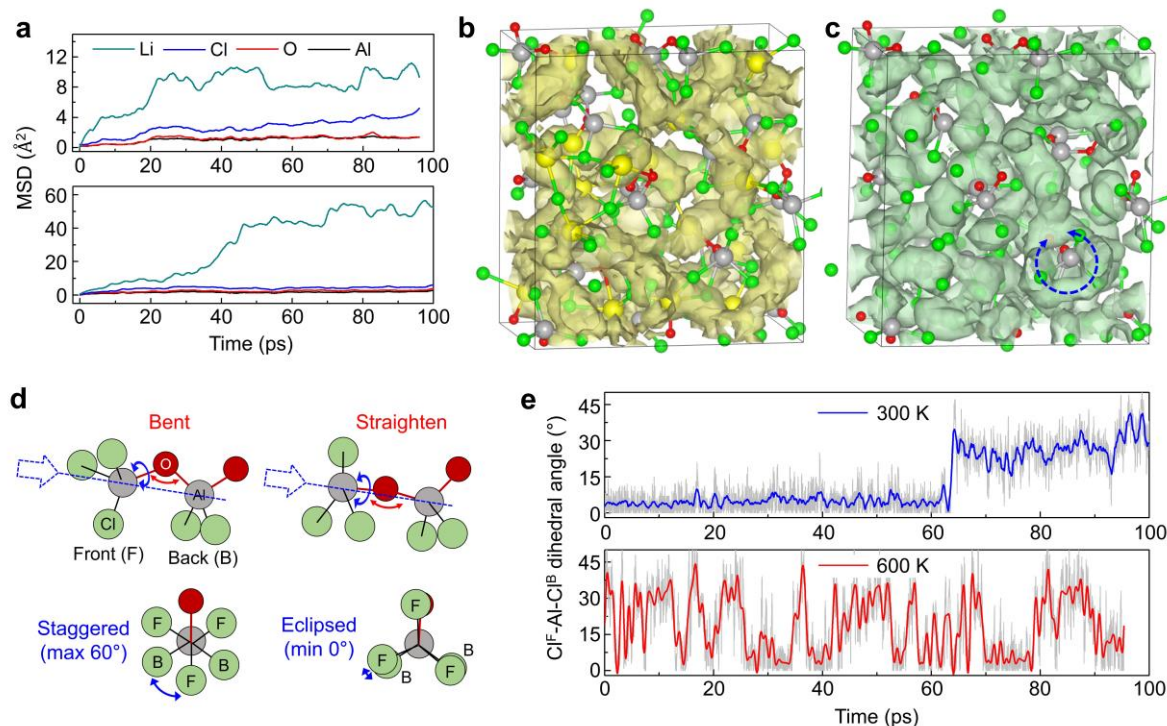

Figure 4. Conformational dynamics in AIMD-simulated LAOC model. (a) the MSD of each element in the LAOC^{0b} supercell during AIMD simulation at 400 K (top) and 600 K (bottom). **(b,c)** isosurface of Li (b) and Cl (c) during AIMD simulation at 600 K showing the Li-ion conductive path that is formed; Cl shows rotational motion as noted by the blue circles. The isosurface value was set to 2.0×10^{-4}. **(d)** Visualization of characteristic angles in LAOC^{0b}. Al-O-Al angle (top, red) reflects the bending motion and the Cl^F-Al-Cl^B dihedral angle (bottom, blue) reflects rotational motion. **(e)** Cl^F-Al-Cl^B angle variations during 100 ps AIMD simulation at 300 K (top) and 600 K (bottom). Low-pass filter (1 Hz) was applied to the original plots (gray-colored) to display rotational motion.

analysis of the dihedral angle formed by the terminal Cl. The angle serves as a general descriptor for rotational states within organic polymeric structures.[43,44] In LAOC, the Cl^F-Al-Cl^B dihedral angle varies between 0° (eclipsed) and 60° (staggered) in conjunction with the bending of the Al-O-Al backbone (**Fig. 4d**) (see **Fig. S17**, **S18** for details). Despite the short snapshot duration of 100 ps, observable angular transitions occurred even at 300 K (**Fig. 4e**, top) (**Movie S1**), demonstrating facile dynamics. At 600 K, the angle underwent significantly more dynamic variation as expected (**Fig. 4e**, bottom) (**Movie S2**). The rotational motion entails transitions between discrete angles, rather than gradual changes.

Rotational motion of oligomer and mechanical plasticity
Rotational, stretching, and slippage motions observed in polymeric (oligomeric) glasses are widely acknowledged mechanisms that contribute to mechanical plasticity by facilitating the formation of local free volume.[45,46] These theories have been formulated based on numerical models of segmented structures, irrespective to the constituent elements, leading us to posit that the 'plasticity mechanism' applies to oligomeric LAOC.

First, we simulated the stress-strain curve of oligomeric solid based on $LAOC^{0b}$ model using the trained DeepMD potential (See Experimental for details). With respect to tensile stress, it showed an elastic region up to 5 % strain with a modulus of ~3 GPa at RT (**Fig. S19a**), which is comparable to the value of ~2 GPa reported in a previous study of other lithium aluminum oxychlorides measured by dynamic mechanical analysis.[20] Beyond the strain of the elastic

region, LAOC entered the plastic region with a yield stress of 0.15 GPa. Additionally, it showed a similar yield stress (0.17 GPa) to shear force (**Fig. S19b**), which is much lower than that of a simulated $LiCl-GaF_3$ glass (0.5 GPa) that demonstrates a shear-transformation-zone.[19]

A classic signature of rotational motion is a second-order phase transition observed through a heat capacity measurement. Goldstein proposed that molecular glasses exhibit a glass transition due to additional configurational entropy - primarily steming from molecular rearrangements - along with vibrational entropy,[47] which has been extensively applied to different materials such as metallic glasses[48] and glass-forming liquids.[49] Since rearrangement of an oligomeric structure is provoked by rotation as described by the plasticity mechanism, a glass transition may serve as an indication of rotational motion. All $LAOC^{1.5b/1b/0.3b}$ show a T_g around -15 °C, measured by differential scanning calorimetry (DSC) (**Fig. 5a**), wherein fully unsaturated $LAOC^{2b}$ does not exhibit a glass transition. This can be explained because rotational motion cannot occur with bridging Cl.

To evaluate the effect of mechanical plasticity, the ionic conductivity of particulate $LAOC^{1.5b}$, $LiAlCl_4$ and Li_6PS_5Cl was measured as a function of pressure (**Fig. 5b**) (**Fig. S20**). Unlike $LiAlCl_4$ and Li_6PS_5Cl whose slopes did not saturate even at 85 MPa, the conductivity of $LAOC^{1.5b}$ reached saturation around 60 MPa, indicating its lower elastic modulus (or yield stress). The plasticity of $LAOC^{1.5b}$ enables maintenance of intimate contact between solid particles after releasing the pressure, resulting in invariant conductivity. In contrast, the other two SSEs experienced a loss of conductivity due to elasticity.
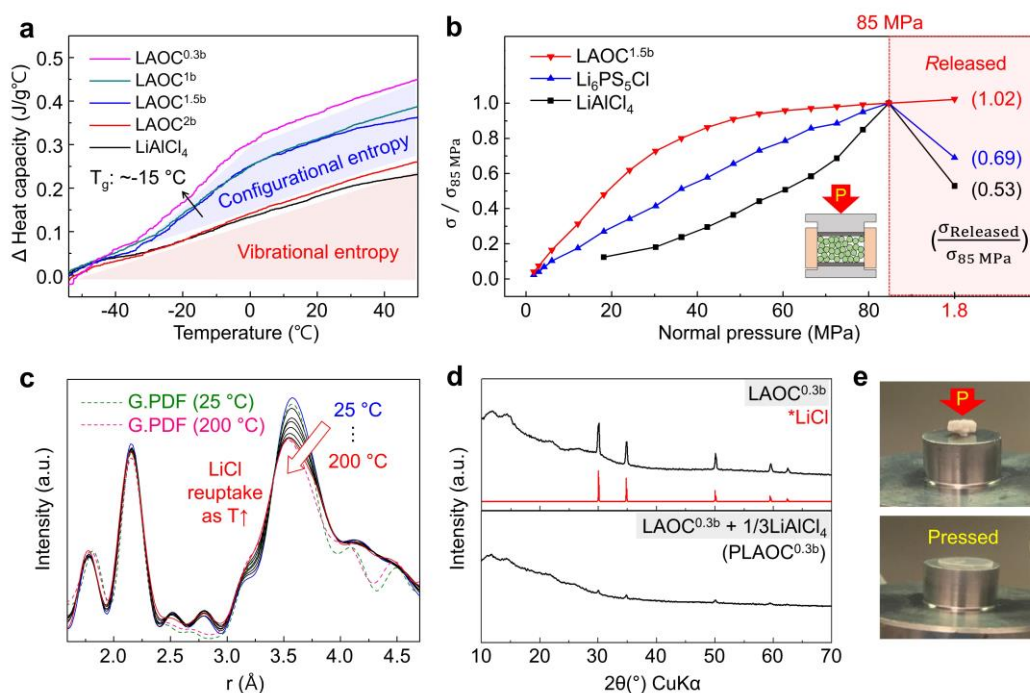

Figure 5. Entropy and plasticity of LAOC. (a) Heat capacity of $LiAlCl_4$ and LAOC as a function of temperature, measured by DSC. **(b)** Pressure-responsive ionic conductivity of particulate solid-state electrolytes. The conductivity (σ) was normalized based on the value at 85 MPa (σ_{85MPa}). The point in the "released segment" denotes the value after releasing the pressure to 1.8 MPa. **(c)** High temperature PDF analysis of $PLAOC^{0.3b}$ showing LiCl re-uptake in the temperature range from 25 °C to 200 °C. With simulated $LAOC^{0b}$ and LiCl structures, PDF plots were generated (G.PDF) to fit the observed PDF at 25 °C and 200 °C. **(d)** XRD patterns showing plasticization of $LAOC^{0.3b}$ by incorporation of $LiAlCl_4$. XRD patterns in red is simulated. **(e)** Images showing the plasticity. Heated $PLAOC^{0.3b}$ was pressed at 10 MPa before cooling it down.

ARTICLE

In LAOC, greater plasticity is expected with a higher degree of Cl saturation that enables Cl rotation, but this induces formation of LiCl (**Fig. 1c**). To prevent such phase-separation, an excess of LiAlCl$_4$ was added to LAOC$^{0.3b}$ (see Experimental). The AlCl$_4^-$ anion, intervening between the saturated trimers, plays a role as a plasticizer. Because the trimers can maintain their saturated state in plasticized LAOC$^{0.3b}$ - allowing rotational motion - PLAOC$^{0.3b}$ is a clay-like viscous solid at elevated temperatures (**Fig. S21**, **Movie S3**). This softening arises from the enhanced dynamics (rotational and slippage motion) of the oligomers, facilitating the reaction kinetics of LiCl uptake in LAOC$^{0.3b}$ trimers, as observed *via* PDF analysis. As the temperature increases, the intensity of the Cl-Cl^{1st} peak decreases due to the reduced amount of LiCl, and thereby the content of LiCl in the generated PDF with the simulated LAOC^{0b} decreases from 12.2 % (25 °C, R_w=0.229) to 6.3 % (200 °C, R_w=0.238) (**Fig. 5c**). Such LiCl uptake is evidence of an equilibrium among the LAOC trimers that is driven to the left in **Fig. 1a** and implies the higher thermodynamic stability of the saturated trimer at elevated temperatures due to conformational entropy, compared to the unsaturated case. This results in a significant decrease in the LiCl XRD peak intensity even at RT (**Fig. 5d**).

As shown by XRD, LiAlCl$_4$ in PLAOC$^{0.3b}$ (LAOC$^{0.3b}$:LiAlCl$_4$ = 3:1) does not precipitate as a crystalline phase, although the AlCl$_4^-$ anion was observed by Raman spectroscopy (**Fig. S11b**) and DSC (**Fig. S21a**). In contrast, it does precipitate as a crystalline phase when an excess amount of LiAlCl$_4$ (LAOC$^{0.3b}$:LiAlCl$_4$ = 3:4) is used (**Fig. S21b**). This indicates that in PLAOC$^{0.3b}$, the entropy gained from the distribution of the AlCl$_4^-$ anion among the trimers predominates over enthalpy (i.e., the crystallization of LiAlCl$_4$). We propose this hinders interaction between the saturated trimers, thereby suppressing the phase separation of bulk LiCl from them. Also, it is notable that the trimers do not react with the excess LiAlCl$_4$ to form oligomers with a higher Al/O ratio (e.g., 4/2), owing to their thermodynamic stability. Therefore, PLAOC$^{0.3b}$ shows comparable ion conductivity (1.2 mS/cm) to LAOC$^{1.5b}$ (**Fig. S2, S22**), despite being in a metastable state. Heated PLAOC$^{0.3b}$ is easily reshaped due to its viscoplastic nature (**Fig. 5e**). Since LAOC benefits from heat-induced viscoplasticity, the thermal stability of LAOC$^{1.5b}$ was checked by aging the material at 150 °C for 12 hours after synthesis, which resulted in a minimal change in ion conductivity (from 1.29 to 1.15 mS/cm) (**Fig. S23**).
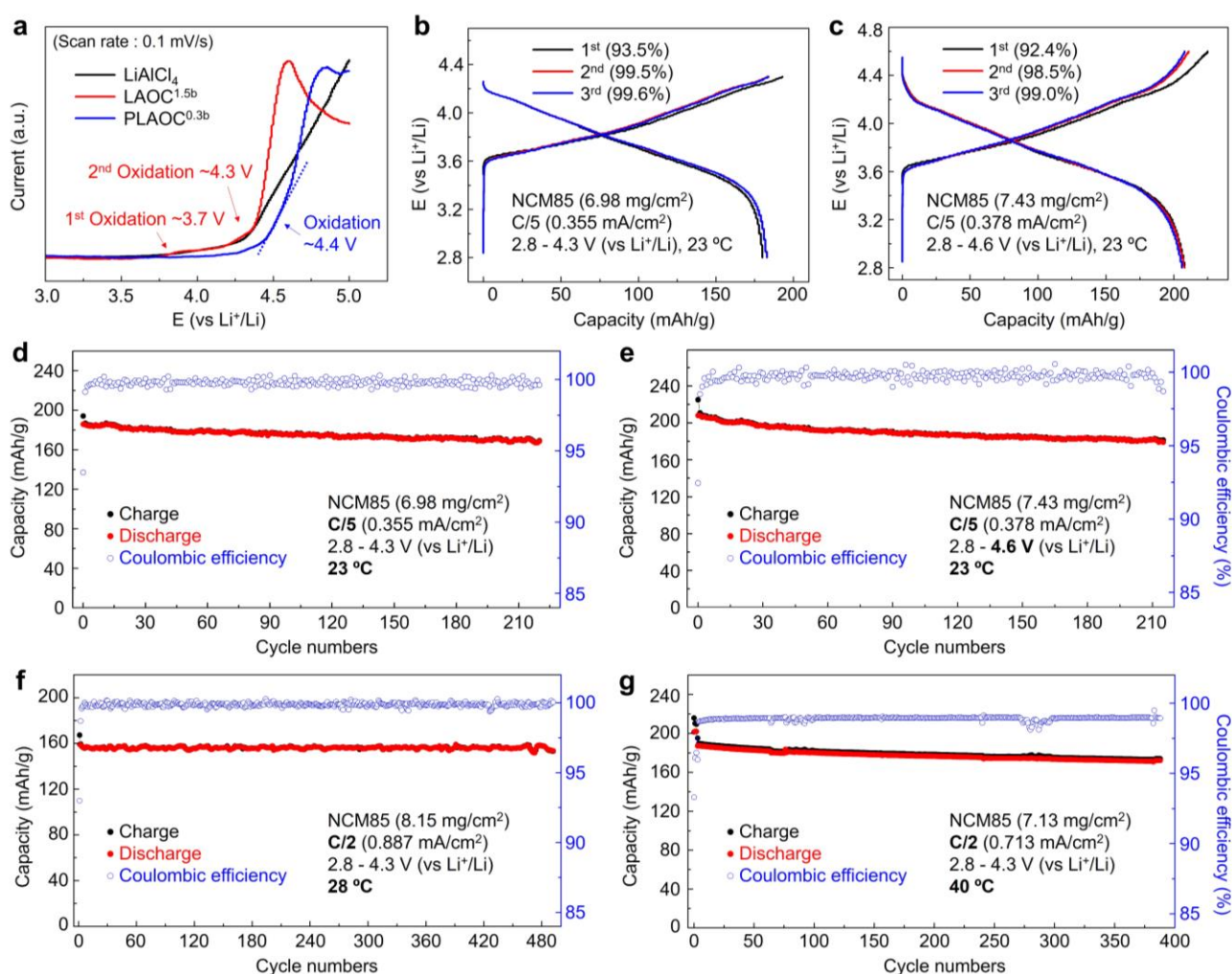

Figure 6. Electrochemical properties of PLAOC$^{0.3b}$. (a) Linear sweep voltammetry of LiAlCl$_4$, LAOC$^{1.5b}$ and PLAOC$^{0.3b}$. **(b,c)** Initial charge-discharge curves of ASSBs whose cathode composite was composed of NCM85 and PLAOC$^{0.3b}$. Cells were charged up to 4.3 V (b) and 4.6 V (c), and run at a C/5 rate; **(d,e)** Charge-discharge capacity at C/5 of cell, charged up to 4.3 V (d) and 4.6 V (e) at 23 °C. **(f,g)** Long term charge-discharge capacity at C/2, charged up to 4.3V at 28 °C (f) and at 40 °C (g). The initial 3 cycles of (g) were run at C/5. The 1C rate is defined as a capacity of 200 mAh/g.

Electrochemical properties and ASSB demonstration

The electrochemical properties were analysed using linear sweep voltammetry (LSV) of ASSB cells. The oxidation potential of LAOC[1.5b] was comparable to that of LiAlCl$_4$ (4.3 V), while saturated PLAOC[0.3b] showed higher stability (4.4 V, **Fig. 6a).** Expanded plots for the anodic and cathodic sweep showing absolute current values are given in **Fig. S24**). We fabricated ASSBs with a high-nickel cathode-active material (NCM85) and PLAOC[0.3b] as the solid catholyte. The high anodic stability of PLAOC[0.3b] does not require any coating on cathode materials run with a high cutoff potential (4.3 V, and even up to 4.6 V).[50] Its long-term electrochemical stability against a high-nickel cathode-active material (NCM85) was confirmed through ASSB cell studies (NMC85: PLAOC[0.3b] = 80:20 wt%). ASSBs run at 0.1C delivered a capacity of 206 mAh.g^{-1}, close to the typical maximum capacity of NCM85 (210 mAh.g^{-1}; see **Fig. S25a** for rate studies). At a C/5 rate at room temperature, the ASSBs showed very high coulombic efficiency (CE) starting from the initial cycle at both 4.3 V (**Fig. 6b**) and 4.6 V (**Fig. 6c**), with capacities on the order of 180-200 mAh.g^{-1} and very good stability over > 200 cycles (**Fig. 6d,e,** respectively). Longer-term cycling at a C/2 rate revealed excellent electrochemical stability over 400 cycles at 28 °C (**Fig. 6f**). Cell cycling at an elevated temperature (40 °C) exhibited improved capacity and very good long-term stability over 400 cycles (**Fig 6g**). LAOC[1.5b] also exhibited good electrochemical performance over > 300 cycles (**Fig. S25b**).

Although this work focusses on the fundamental characteristics of LAOC, we also tested the feasibility of low-pressure cell operation, benefiting from the plasticity of LAOC. Notably, PLAOC[0.3b] forms a negligible gap with NMC85 particles after ASSB cell fabrication, in contrast to crystalline LiAlCl$_4$, as observed in cross-sectional scanning electron microscopy images (**Fig. S26**). This was consistent with the low impedance of the cell retained at low pressure (**Fig. S27a**), indicating that its electrical and ionic conduction paths were conserved due to the plasticity. The ASSB cell operated under 3 MPa exhibited good cycling stability (94 % capacity retention after 70 cycles) (**Fig. S27b**), albeit with slightly lower capacity (~125 mAh.g^{-1} at a C/2 rate, 23 °C). A processing study to optimize a homogeneous cathode composite made with plastic SSE, carbon, and binder is underway to improve the energy density of ASSBs operable under low pressure, although this is beyond the scope of the current work.

Conclusions and outlook

In this work, we demonstrate a lithium aluminium oxychloride SSE based on oligomer design that shows high conductivity (> 1 mS/cm at 30 °C), high oxidation stability (> 4.3 V vs Li$^+$/Li) and mechanical plasticity, obtained through a scalable and cost-effective synthesis process. Drawing from its oligomeric structure, unlike the previously reported inorganic soft electrolytes, the physical origin of its mechanical plasticity is effectively explained by conformational dynamics. The mechanical properties of polymers are due to similar chain dynamics above T$_g$, but LAOC exhibits a high Li transference number (close to 1.0), in contrast to polymer electrolytes.[51]

LAOC exhibits three distinct peaks in its ^{7}Li-ssNMR spectrum, suggesting that Li ions do not undergo rapid site exchange which would lead to merging of all the signals. This suggests that Li ions in LAOC migrate through hopping between sites instead of by a "vehicular mechanism" exhibited in polymer electrolytes.[52] Therefore, 3D ion migration in LAOC is influenced by the size of the ions, particularly in overcoming the energy barrier of spatial bottlenecks. This contributes to the low mobility of bulky anions in LAOC compared to Li cations. We also synthesized a sodium ion conductor (plasticized Na-AOC[0.3b], PNAOC[0.3b]) and a sodium-potassium mixed ion conductor (plasticized Na$_{0.75}$K$_{0.25}$-AOC[0.3b]) using the same method. The low melting point (129 °C) of the eutectic 0.75NaAlCl$_4$–0.25KAlCl$_4$ phase[53] facilitated the synthesis process, but the larger size of K$^+$ results in reduced conductivity of the mixed ion conductor (0.064 mS/cm) compared to PNAOC[0.3b] (0.8 mS/cm) and PLAOC[0.3b] (1.2 mS/cm) at 30 °C (**Fig. S28**). This work will be presented in detail elsewhere.

The Li conductivity enhancement in LAOC, facilitated by the introduction of oxygen, is in line with recent studies that have highlighted the impact of mixed-coordination[3,4] and geometrical frustration[5,6] in various SSEs. Unlike the previous studies, however, the enhanced ion conductivity of LAOC is not attributed to a smoother energy landscape, given its comparable activation energy (0.46~0.47 eV) to that of LiAlCl$_4$ (**Fig. S2**). It implies that the conductivity boost is primarily driven by an increased attempt frequency (v_0) or entropy (ΔS) for Li hopping, which determine the prefactor ($\sigma_0 = A e^{\Delta S/k_B} a_0^2 v_0$) in the Arrhenius equation.[54] Any change in the jump distance (a_0), generally dictated by the nearest Li-Li distances in solids, could not account for the 10^3-fold increase in conductivity. Although additional conformational entropy (a part of configurational entropy) was introduced through rotational motion, as indicated by the glass transition, further study is required to elucidate the specific correlation between Li dynamics and structure.

We note that the LAOC structure is also analogous to semi-crystalline LiNbOCl$_4$ (LiTaOCl$_4$) which exhibits a polymeric structure and high ion conductivity (>10 mS/cm at RT).[55,56] Both structures feature a linear metal-oxygen-metal backbone; while the relatively straight backbone ($\angle$O-Nb-O ~160°) deviates from the distorted backbone ($\angle$O-Al-O ~110°) of LAOC due to the different coordination geometries of the central metals (i.e. octahedral Nb vs tetrahedral Al). The structural resemblance suggests the potential for other diverse oligomeric configurations.

Since simulating non-periodic structures is quite challenging, oligomer-based SSE have not been anticipated in cutting-edge material research that aims at discovering new SSEs via *ab-initio* calculations and machine learning.[57,58] We believe that design from the oligomeric structure, as a building block of solids, will be a promising research avenue in discovering new SSEs. This work can serve as a cornerstone in the development of plastic solid-state electrolytes.

Experimental

Chemicals.

Lithium chloride (LiCl, anhydrous, 99.95%), sodium chloride (NaCl, 99.99%), potassium chloride (KCl, 99%) and aluminium chloride (AlCl$_3$, ultra-dry, 99.99%) were purchased from Thermo Fisher Scientific, and [7]LiCl, aluminium chloride hexahydrate (AlCl$_3$·6H$_2$O, 99%), lithium aluminium oxide (LiAlO$_2$), lithium oxide (Li$_2$O),

acetonitrile (anhydrous, 99.8%) and 1-Methyl-2-pyrrolidinone (anhydrous, 99.5%) were purchased from Sigma Aldrich. $LiNi_{0.85}Co_{0.1}Mn_{0.05}O_2$ (NCM85, D50 = 4 μm) cathode powder was provided from BASF and used as received. Argyrodite (Li_6PS_5Cl, 1 μm) was purchased from MSE supplies. All the chemicals were stored in an Ar-filled glove box.

Synthesis.

To synthesize crystalline $LiAlCl_4$: LiCl and $AlCl_3$ powders were placed into a quartz tube and sealed under vacuum. The quartz tube was annealed at 200 °C for 20 hours, during which the powder turned into a liquid. The solid $LiAlCl_4$ was collected after cooling and ground into a powder for the next step. To synthesize LAOC: $LiAlCl_4$, $AlCl_3$ and $AlCl_3 \cdot 6H_2O$ powders (around 1 g) were ground by hand at the target molar ratio and annealed for 2 hours at 190 °C under vacuum. HCl gas was released during the process. We note that the reactants for unsaturated LAOC, such as $LAOC^{1.5b}$, turns into liquid during grinding. The liquid becomes plastic solid after releasing HCl. After cooling, the material was collected and ground into powder for further study. $Li_2Al_2O_2Cl_{10}$ was synthesized according to its composition (i.e. $6LiAlCl_4$ + $5AlCl_3$ + $AlCl_3 \cdot 6H_2O \rightarrow 3Li_2Al_2O_2Cl_{10}$ + 12HCl). For the synthesis of $PLAOC^{0.3b}$, an additional amount of $LiAlCl_4$ was added to the condition of $LAOC^{0.3b}$ synthesis (i.e. $9LiAlCl_4$ + $AlCl_3 \cdot 6H_2O \rightarrow 2LAOC^{0b}$ + $LAOC^{1b}$ + $LiAlCl_4$ + 12HCl). To synthesize $NaAlCl_4$; NaCl and $AlCl_3$ powders were placed into a quartz tube and sealed under vacuum. The quartz was annealed at 200 °C for 20 hours and then the solid $NaAlCl_4$ was ground into a powder. To synthesize NAOC, $NaAlCl_4$, $AlCl_3$ and $AlCl_3 \cdot 6H_2O$ powders were ground by hand at the target molar ratio and annealed for 2 hours at 190 °C under vacuum. To synthesize $Na_{0.75}K_{0.25}AlCl4$; NaCl, KCl and $AlCl_3$ powders were placed into a quartz tube and sealed under vacuum. The quartz was annealed at 200 °C for 20 hours and then the solid $Na_{0.75}K_{0.25}AlCl_4$ was ground into a powder. To synthesize $Na_{0.75}K_{0.25}AOC$, $Na_{0.75}K_{0.25}AlCl_4$, $AlCl_3$ and $AlCl_3 \cdot 6H_2O$ powders were ground by hand at the target molar ratio and annealed for 2 hours at 190 °C under vacuum. The reactants were placed in a PTFE beaker (or bottle), and the vacuum annealing process was performed using a Buchi glass oven connected to a Schlenk line. For the synthesis of Li_5AlO_4, $LiAlO_2$ and Li_2O were ground in a 1:2 mole ratio and pelletized. The pellet was annealed at 700 °C for 48 hours in a vacuum-sealed quartz tube enclosed with the amorphous carbon crucible. All the reactants were prepared and processed inside Ar-filled glove box (H_2O < 0.5 ppm).

X-ray powder diffraction.

Powder X-ray diffraction measurements were conducted at RT on a Panalytical Empyrean diffractometer employing CuKα radiation. A PIXcel line detector was used. X-ray diffraction patterns were obtained in Bragg–Brentano geometry, with samples placed on a zero-background sample holder in an Ar-filled glovebox and protected by a thin Kapton film. The XRD pattern of $Li_2Al_4O_2Cl_{10}$ was measured in Debye–Scherrer geometry with long scan times (2 h/scan, averaged from 8 scans to improve counting statistics), with the sample sealed in 0.5 mm (diameter) glass capillaries under Ar.

X-ray synchrotron total scattering & data reduction.

Synchrotron total scattering was conducted at the Brockhouse Diffraction Sector Beamline at the Canadian Light Source (CLS). The X-ray energy was 60.83 keV and the data was collected to a Q_{max} of 25 Å⁻¹. $LAOC^{1.5b}$ and $LAOC^{0.3b}$ were measured in flat plate geometry in the pellet form (1 mm thickness), encapsulated by Kapton film (8 μm). All the samples were prepared inside an Ar-filled glove box. Temperature-dependent PDF for $PLAOC^{0.3b}$ was measured in Debye–Scherrer geometry, with the samples sealed in 1 mm (diameter) glass capillaries. A Varex 2D detector consisting of 2880 x 2880 pixels was used. Temperature was changed using an Oxford Cryostream furnace, which can rapidly reach the desired temperature. A thermostat was placed inside the capillary to ensure that temperature was accurately measured. Data reduction was conducted in GSAS-II software and transformed to PDF. The background was subtracted from the total scattering pattern. The Fourier-transformed range Q_{max} was around 24 Å⁻¹.

X-ray absorption spectroscopy.

XAS analysis was conducted at the Spherical Grating Monochromator Beamline at CLS. Partial fluorescence yield for oxygen K-edge was collected at the Spherical Grating Monochromator (SGM) beamline using a four-element silicon-drift-detector array. The samples were transferred through a special sealed chamber from the glovebox to ensure an air free environment. The data was processed through Athena.

Rietveld refinement & PDF small box modelling

Rietveld refinement against X-ray data was carried out using the GSAS-II software package.[59] The initial structural model for $Li_2Al_4O_2Cl_{10}$ was derived from the $Ag_2Al_4O_2Cl_{10}$ crystal structure by replacing Ag ions with Li ions, followed by DFT-relaxation. A Chebyshev-1 function with 30 coefficients was used for fitting the background. Lattice parameters, scale factors, atomic coordinates, particle size and atomic displacement parameters were sequentially refined. Synchrotron PDF data were modelled using PDFfit2 source code embedded in the PDFgui software package.[60] A standard Ni sample was fit to obtain Q_{damp} and Q_{broad} parameters. Two structural models were used for the fitting; one was crystalline LiCl and the other one was AIMD-simulated $LAOC^{0b}$. Initial fitting in the range between 10 to 30 Å was conducted only with the LiCl model to determine the lattice parameters and scale factor of LiCl. Since Li rarely responds to synchrotron X-ray, the occupancy of Li in LiCl model was not considered for generating PDF. After fixing the parameters for LiCl and changing the fitting range to 1.0 Å to 4.7 Å, the simulated $LAOC^{0b}$ model was added for the fitting. The lattice parameters and scale factor for $LAOC^{0b}$ were refined. The quantity of LiCl was estimated based on the ratio of scale factors from LiCl and $LAOC^{0b}$, representing the weight ratio. PDF fitting for $PNAOC^{0.3b}$ was conducted in the same manner.

Characterization.

Fourier-transform infrared spectra were measured on a Bruker Hyperion 3000 FTIR Microscope in transmission mode. The target samples were incorporated in a KBr pellet at 0.3 wt%. The analysis was carried out quickly to minimize air exposure. Raman spectroscopy measurements were performed using a Renishaw inVia Reflex system equipped with a sample stage capable of 100 nm positioning in three dimensions. A 532 nm (Renishaw DPSSL laser, 50 mW) laser filtered to 1 % intensity was focused on the samples. The

samples were encapsulated by a cover glass, glass slide and epoxy for airtight analysis. Samples for DSC were encapsulated in an aluminium pan and scanned at a rate of 10 K/min. The observed heat capacity was calibrated with a sapphire reference. TGA was conducted using an alumina crucible and scanned at a rate of 10 K/min under nitrogen atmosphere. ssNMR was measured with Bruker 850HD spectrometer (20 T) using a 1.9 mm double resonance probe, at a MAS spinning rate of 20 kHz. All the ^{7}Li spectra were referenced to solid LiCl at -1.1 ppm.[39] Electrospray Ionization was performed with a ThermoFisher Scientific LTQ linear ion trap mass spectrometer. Samples were dissolved in anhydrous acetonitrile (50 μmol/L) and infused at 10 μL/min with nitrogen. Spray voltage was 3 kV and nominal mass was acquired over a 50 to 1000 (m/z) range. The simulated nominal masses and isotopic distributions were obtained from Chemcalc (chemcalc.org). All the samples were prepared inside Ar-filled glove box (H_2O < 0.5 ppm).

Ab-initio simulations.
We employed *ab* initio density functional theory (DFT) and molecular dynamics (AIMD) simulations to investigate the local structure of anion framework and Li-ion dynamics. The initial model for molecular structures of $[Al_3O_2Cl_8]^{3-}$ was obtained from known $Si_3O_2Cl_8$[23] while other unsaturated trimers such as $[Al_3O_2Cl_7]^{2-}$ and $[Al_3O_2Cl_6]^{-}$ were generated from $[Al_3O_2Cl_8]^{3-}$ by removing one and two Cl atoms from the chain ends, respectively. All the trimeric oligomers were first geometry optimized using the Gaussian 16 (G16) package[61] with a hybrid functional B3LYP and the 6-31G (d, p) basis set followed by DFT structural relaxation using Vienna *ab* initio simulation package (VASP).[62,63] We utilized planewave pseudopotentials with projector augmented wave (PAW) to account for core electrons, while the Perdew–Burke–Ernzerhof (PBE) version within the generalized gradient approximation (GGA) was employed for the exchange-correlation term.[64] The DFT calculations were performed with a plane wave energy cutoff of 520 eV. To ensure accuracy, the total energy and forces converged to 10^{-5} eV and 0.01 eV/A, respectively, during geometry optimization.

The oligomeric LAOC structure was generated from the chain-like framework of $LiNbOCl_4$[56] by substituting Nb for Al and selectively removing excess Cl atoms while restricting the supercell dimensions to the experimentally observed density, 1.9 g/cm^3. The generated structural model was thus relaxed using DFT calculations at a fixed volume. The simulation supercell was made up of 8 oligomer units of $Li_3Al_3O_2Cl_8$ or $Li_2Al_3O_2Cl_7$ and contained 128 and 112 atoms, respectively. The supercell was then simulated using AIMD simulations for melting at 600 K for 10 ps and quenched at 300 K for 10 ps to obtain the final structural model. The AIMD simulations were performed in the NVT ensemble, where temperature was controlled using a Nosé–Hoover thermostat.[65] The time step for AIMD simulations was 1 fs. A Γ-centered k-point mesh was used. The dispersion interactions between the oligomeric chains were considered using the DFT-D3 method of Grimme. Similarly, the amorphous LAOC was obtained by replacing some of the Cl atoms in the 2x2x1 supercell of $LiAlCl_4$ (*P21/c*) by O atoms to generate a LAOC composition and DFT relaxation was performed at a restricted volume corresponding to the experimental density (1.9 g/cm^3) of LAOC. A similar melt quench procedure was used following the DFT relaxation.

At each temperature (300 K - 800 K), the DFT relaxed structure was first equilibrated for 10 ps with time step of 1 fs before starting the production run with time step 2 fs and the trajectories of all lithium ions were tracked for ~100 ps. The self-diffusivity (D) of the Li ion was evaluated using the mean squared displacement (MSD) over time in accordance with the Einstein relation:[66]

$$D(T) = \frac{1}{2dN\Delta t} \sum_{i=1}^{N} \langle [r_i(t + \Delta t) - r_i(t)]^2 \rangle_t$$

where d is the dimension of the diffusion, N is the total number of diffusing ions, and $r_i(t)$ is the displacement of the ith ion at time t.

The conductivity (σ_i) can be approximated from self-diffusivity assuming dilute, isolated mobile-ion carriers using the Nernst–Einstein relation,

$$\sigma = \frac{nq^2 D}{K_B T}$$

where K_B is Boltzmann constant, n is the mobile ion's volume density and q (+1 for Li) is the ionic charge. AIMD simulations were analysed using the pymatgen-diffusion add-on package.[67] The Li-ion diffusion pathways were obtained by calculating the probability density function through averaging the number of Li-ions at each point in a uniform spatial grid for a given time frame. The conformation analysis was performed by a python script which utilizes the library polyhedral.[68]

Dihedral angle observation with AIMD simulation.
Cl^B-Al-Cl^F dihedral angles were tracked during the 100 ps of AIMD simulation based on LAOC^{0b} model. The dihedral angle is the angle between two intersecting planes formed by Cl^B-Al and Cl^F-Al. The angles were tracked based on the oxygen that bridges the two Al as a geometric reference point, with a total of sixteen oxygen atoms in the simulated supercell containing eight LAOC^{0b} (two oxygens in each LAOC^{0b}). We specifically examined the minimum angle among the various combinations of Cl^B-Al-Cl^F dihedral angles formed at each Al-O-Al moiety. To observe the dynamics of the dihedral angles at a frequency below 1 THz, a low-pass fast Fourier transform (FFT) filter with a cut-off frequency of 1 Hz was applied to the plots, presented on a pico-second scale.

Simulation of mechanical properties using DeepMD.
To simulate the mechanical behaviour of $Li_3Al_3O_2Cl_8$ over extended length and time scales, we developed an interatomic potential using data from AIMD simulations, trained with neural network algorithm as implemented in the DeepMD-kit package.[69] A 10.0 Å cut-off was applied for neighbouring atom interactions, and the embedding and fitting network sizes were set to (25, 50, 100) and (240, 240, 240), respectively. The potential model was trained on 50,000 AIMD frames and validated on 4,000 frames, selected from a total of 500,000 frames. These frames were generated from annealing, quenching, and equilibration processes across a temperature range of 300 K to 700 K, applied to both the unit cell (128 atoms) and a 1x1x2 supercell (256 atoms). Training was conducted over 10^6 iterations to minimize the loss function. The root mean square errors (RMSE) for the final potential were <1 meV/atom for energy and <48 meV/Å for forces.

The mechanical properties of $Li_3Al_3O_2Cl_8$ were investigated through MD simulations using the LAMMPS package[70] with the trained DeepMD potential model. Simulations were performed on a large supercell containing 16,384 atoms, with lattice dimensions ranging from 60 to 80 Å. The system was equilibrated at 300 K for 100 ps in the NVT ensemble, followed by another 100 ps equilibration at 300 K and zero pressure in the NPT ensemble. We used a Nose-Hoover thermostat with a time step of 1 fs, and damping parameters for temperature and pressure set to 0.1 ps and 1 ps, respectively. For the shear stress-strain calculations,[19] constant strain rate MD simulations were performed at 300 K, with the simulation cell deformed on the yz-plane under a strain rate of 10^{-3} ps^{-1}, while maintaining zero pressure in all other boundaries using the NPT ensemble. For the tensile stress-strain calculations, constant strain rate (10^{-3} ps^{-1}) was applied on x-axis at 300 K using the NPT ensemble under same conditions with shear test.

Impedance spectroscopy in various temperature and pressure.
Ionic conductivity was measured by electrical impedance spectroscopy (EIS). Generally, 100 mg of the SSE powder was placed between two titanium rods and pressed into a 10 mm diameter pellet by a hydraulic press in an Ar-filled glovebox. EIS experiments were performed with 100 mV constant voltage within a frequency range of 1 MHz to 100 mHz using a VMP3 potentiostat/galvanostat (BioLogic). For activation energy measurements, ~100 mg of LAOC powder was placed between titanium rods and pressed into a 10 mm diameter pellet in a custom-made cell, and indium foil was placed on both sides to eliminate the contact resistance. The cell was then placed in a custom-made cage to maintain the pressure. The impedance was measured from 3 MHz to 1 Hz at temperatures ranging from -60 to 70 °C using an MTZ-35 impedance analyser (BioLogic). For pressure-sensitive conductivity measurements, ~100 mg of SSE powders ($LAOC^{1.5b}$, $LiAlCl_4$ and Li_6PS_5Cl) were placed between titanium rods in the same configuration for the activation energy measurement. The cell was placed in a custom-made cage capable of applying pressure using torque wrench. EIS was measured incrementally, increasing the pressure up to 85 MPa, followed by a measurement at 1.8 MPa after releasing the pressure.

Transference number measurement.
The transference number was measured by the Watanabe method[26] using the equation $t_{Li^+} = I_{ss}R^b/(\Delta V - I_{ss}R_{ss}^{int})$, where I_{ss} is the steady state current, R^b is the bulk resistance of SSE and R_{ss}^{int} is the interface resistance at the steady state. To obtain a stable steady state current, a thin Li_6PS_5Cl layer (< 200 μm) was used as the interlayer between the $LAOC^{1.5b}$ (or $PLAOC^{0.3b}$) layer and Li metal on both sides. First, $LAOC^{1.5b}$ (or $PLAOC^{0.3b}$) powders were placed in a 10 mm PEEK die and pressed at 0.5 ton (> 4000 μm). Then Li_6PS_5Cl powder was spread over on both sides and pressed at 200 MPa sequentially. Since Li_6PS_5Cl is more conductive and its layer is much thinner than LAOC, R^b was governed by $LAOC^{1.5b}$ (or $PLAOC^{0.3b}$). After laminating Li metals on both sides, 20 MPa of pressure was applied during the measurement. I_{ss} was obtained after a 1 hour of DC polarization (chronoamperometry, ΔV=100 mV). R^b was measured by AC impedance spectroscopy (1 MHz – 0.1 Hz) after the polarization. R_{ss}^{int} between Li metal and Li_6PS_5Cl was measured using a separately fabricated Li-symmetric cell for Li_6PS_5Cl. This is because interface resistance becomes dominant when the cell has a low bulk resistance, which is favourable for observing R_{ss}^{int}. In a 10 mm PEEK die, Li_6PS_5Cl powder was pressed with 200 MPa. After the lamination of Li metals on both sides, 20 MPa of pressure was applied during the measurement. R_{ss}^{int} was measured by impedance spectroscopy after a 1 hour of DC polarization (chronopotentiometry) with the current approximately equal to the observed I_{ss} (ΔI= 150 μA) at the LAOC cell. To avoid overestimating R_{ss}^{int}, fresh Li metal foils were used for Li symmetric cell fabrication.

Electrochemical measurements.
ASSBs employing $LAOC^{1.5b}$ or $PLAOC^{0.3b}$ as the solid electrolyte and NMC85 as the cathode were fabricated in an Ar-filled glove box. The cathode composite was formed by mixing LAOC and NMC85 cathode powder (NMC:LAOC=80:20 weight ratio) in a heated mortar (80℃). 80 mg of Li_6PS_5Cl powder (diameter of ~1 μm) was placed in a 10 mm PEEK die and pressed at 0.5 ton with titanium plunger. Then, 40 mg of LAOC powder was spread over the cathode side of a Li_6PS_5Cl pellet and pressed at 0.5 ton. Finally, 7–9 mg of the composite cathode mixture (corresponding to an areal capacity of ~1.0–1.25 mAh cm^{-2}) was spread over the LAOC and pressed at 2 tons for 3 minutes. On the other side of the pellet, an indium foil (10 mm diameter, 99.99%, 0.1 mm thickness), a lithium foil (8 mm diameter, 0.05 mm thickness) and a copper foil (10 mm diameter, 8 μm thickness) were placed in sequence. The fabricated cells were placed into a custom-made stainless-steel casing with an applied pressure of ~200 MPa during cycling to exclude other possible contributions to cycling stability, such as the volume change of NCM. For the low-pressure cell, a pressure of 3 MPa was initially applied using a torque wrench (5 in/lbs). An elastomer film (3 mm) was placed between the plunger and the cell case to accommodate the volume changes of electrodes during cycling. To ensure the reproducibility of the results, at least two cells were employed for each electrochemical test. The cells run at 40 °C were run in a thermostat chamber and the cells run at 28 °C were run inside Ar glovebox.

Author contributions

I.Y. and L.F.N. conceived the material synthesis design and experiment along with characterization. B.S. carried out the AIMD simulations and analysed the data. M.C. and G.G. performed NMR spectroscopy and analysed the data. L.Q. and G.K. collected PDF data, and L.Q. performed the analysis, with help from Yubo Wang (UWaterloo) whom we thank. Z.A. collected the XAS data and helped L.Q. with the analysis. L.F.N. and I.Y. analysed all the data and wrote the manuscript. All authors discussed the results and contributed to the manuscript.

Conflicts of interest

The authors declare no competing interests.

Data availability

The data that support the findings of this study are available from the corresponding author upon reasonable request.

Acknowledgements

References

1   C. Bauer, S. Burkhardt, N. P. Dasgupta, L. A.-W. Ellingsen, L. L. Gaines, H. Hao, R. Hischier, L. Hu, Y. Huang, J. Janek, C. Liang, H. Li, J. Li, Y. Li, Y.-C. Lu, W. Luo, L. F. Nazar, E. A. Olivetti, J. F. Peters, J. L. M. Rupp, M. Weil, J. F. Whitacre and S. Xu, *Nat. Sustain.*, 2022, **5**, 176-178.

2   Y. Ma, J. Wan, X. Xu, A. D. Sendek, S. E. Holmes, B. Ransom, Z. Jiang, P. Zhang, X. Xiao and W. Zhang, *ACS Energy Lett.*, 2023, **8**, 2762-2771.

3   G. Han, A. Vasylenko, L. M. Daniels, C. M. Collins, L. Corti, R. Chen, H. Niu, T. D. Manning, D. Antypov and M. S. Dyer, *Science*, 2024, **383**, 739-745.

4   Y. Deng, C. Eames, B. Fleutot, R. David, J.-N. Chotard, E. Suard, C. Masquelier and M. S. Islam, *ACS Appl. Mater. Interfaces*, 2017, **9**, 7050-7058.

5   K. E. Kweon, J. B. Varley, P. Shea, N. Adelstein, P. Mehta, T. W. Heo, T. J. Udovic, V. Stavila and B. C. Wood, *Chem. Mater.*, 2017, **29**, 9142-9153.

6   B. Kozinsky, S. A. Akhade, P. Hirel, A. Hashibon, C. Elsässer, P. Mehta, A. Logeat and U. Eisele, *Phys. Rev. Lett.*, 2016, **116**, 055901.

7   X. He, Y. Zhu and Y. Mo, *Nat. Commun.*, 2017, **8**, 15893.

8   Y. Zeng, B. Ouyang, J. Liu, Y.-W. Byeon, Z. Cai, L. J. Miara, Y. Wang and G. Ceder, *Science*, 2022, **378**, 1320-1324.

9   K.-H. Park, K. Kaup, A. Assoud, Q. Zhang, X. Wu and L. F. Nazar, *ACS Energy Lett.*, 2020, **5**, 533-539.

10 S. Muy, R. Schlem, Y. Shao-Horn and W. G. Zeier, *Adv. Energy Mater.*, 2021, **11**, 2002787.

11 D. H. Tan, Y. S. Meng and J. Jang, *Joule*, 2022, **6**, 1755-1769.

12 J. Janek and W. G. Zeier, *Nat. Energy*, 2023, **8**, 230-240.

13 J. A. Dawson, P. Canepa, T. Famprikis, C. Masquelier and M. S. Islam, *J. Am. Chem. Soc.*, 2018, **140**, 362-368.

14 Y. Zhu, E. R. Kennedy, B. Yasar, H. Paik, Y. Zhang, Z. D. Hood, M. Scott and J. L. Rupp, *Adv. Mater.*, 2024, **36**, 2302438.

15 R. Schlem, C. F. Burmeister, P. Michalowski, S. Ohno, G. F. Dewald, A. Kwade and W. G. Zeier, *Adv. Energy Mater.*, 2021, **11**, 2101022.

16 S.-K. Jung, H. Gwon, G. Yoon, L. J. Miara, V. Lacivita and J.-S. Kim, *ACS Energy Lett.*, 2021, **6**, 2006-2015.

17 X. Yang, S. Gupta, Y. Chen, D. Sari, H.-M. Hau, Z. Cai, C. Dun, M. Qi, L. Ma, Y. Liu, J. J. Urban and G. Ceder, *Adv. Energy Mater.*, 2024, **14**, 2400163.

18 S. V. Patel, V. Lacivita, H. Liu, E. Truong, Y. Jin, E. Wang, L. Miara, R. Kim, H. Gwon and R. Zhang, *Sci. Adv.*, 2023, **9**, eadj9930.

19 S. Gupta, X. Yang and G. Ceder, *Nat. Commun.*, 2023, **14**, 6884.

20 T. Dai, S. Wu, Y. Lu, Y. Yang, Y. Liu, C. Chang, X. Rong, R. Xiao, J. Zhao and Y. Liu, *Nat. Energy*, 2023, **8**, 1221-1228.

21 S. Zhang, Y. Xu, H. Wu, T. Pang, N. Zhang, C. Zhao, J. Yue, J. Fu, S. Xia and X. Zhu, *Angew. Chem. Int. Ed.*, 2024, **63**, e202401373.

22 N. Flores-González, N. Minafra, G. Dewald, H. Reardon, R. I. Smith, S. Adams, W. G. Zeier and D. H. Gregory, *ACS Mater. Lett.*, 2021, **3**, 652-657.

23 M. Binnewies and H. Borrmann, *Z. Krist-New Cryst. St.*, 2002, **217**, 324-324.

24 L. Malavasi, C. A. Fisher and M. S. Islam, *Chem. Soc. Rev.*, 2010, **39**, 4370-4387.

25 R. W. Berg, H. A. Hjuler and N. J. Bjerrum, *Inorg. Chem.*, 1984, **23**, 557-565.

26 M. Watanabe, S. Nagano, K. Sanui and N. Ogata, *Solid State Ion.*, 1988, **28**, 911-917.

27 L.-Y. Lin and C.-C. Chen, *J. Power Sources*, 2024, **603**, 234236.

28 T. A. Zawodzinski Jr and R. A. Osteryoung, *Inorg. Chem.*, 1990, **29**, 2842-2847.

29 D. Jentsch, P. G. Jones, E. Schwarzmann and G. M. Sheldrick, *Acta Crystallogr. C.*, 1983, **39**, 1173-1174.

30 M.-A. Einarsrud, E. Rytter and M. Ystenes, *Vib. Spectrosc.*, 1990, **1**, 61-68.

31 Z. Wang, C. Li, L. Liu and T.-K. Sham, *J. Chem. Phys.*, 2013, **138**.

32 E. de Clermont Gallerande, D. Cabaret, G. Radtke, C. J. Sahle, J. Ablett, J.-P. Rueff and G. Lelong, *J. Non-Cryst. Solids*, 2020, **528**, 119715.

33 G. Lelong, G. Radtke, L. Cormier, H. Bricha, J.-P. Rueff, J. M. Ablett, D. Cabaret, F. Gelebart and A. Shukla, *Inorg. Chem.*, 2014, **53**, 10903-10908.

34 W. Sun, S. T. Dacek, S. P. Ong, G. Hautier, A. Jain, W. D. Richards, A. C. Gamst, K. A. Persson and G. Ceder, *Sci. Adv.*, 2016, **2**, e1600225.

35 J.-H. Pöhls, M. Heyberger and A. Mar, *J. Solid State Chem.*, 2020, **290**, 121557.

36 V. Kuznetsov, S. Maksimova and A. Morozov, *J. Struct. Chem.*, 1973, **14**, 441-444.

37 R. W. Berg, S. Von Winbush and N. J. Bjerrum, *Inorg. Chem.*, 1980, **19**, 2688-2698.

38 Z. Xu and J. F. Stebbins, *Solid State Nucl. Magn. Reson.*, 1995, **5**, 103-112.

39 B. M. Meyer, N. Leifer, S. Sakamoto, S. G. Greenbaum and C. P. Grey, *Electrochem. Solid-State Lett.*, 2005, **8**, A145.

40 H. Spiesecke and W. G. Schneider, *J. Chem. Phys.*, 1961, **35**, 722-731.

41 N. Tanibata, S. Takimoto, K. Nakano, H. Takeda, M. Nakayama and H. Sumi, *ACS Mater. Lett.*, 2020, **2**, 880-886.

42 Y. Chen, Z. Lun, X. Zhao, K. P. Koirala, L. Li, Y. Sun, C. A. O'Keefe, X. Yang, Z. Cai and C. Wang, *Nat. Mater.*, 2024, **23**, 535-542.

43 N. Gō and H. A. Scheraga, *Macromol.*, 1976, **9**, 535-542.

44 A. Altis, P. H. Nguyen, R. Hegger and G. Stock, *J. Chem. Phys.*, 2007, **126**.

45 L. Anand and M. E. Gurtin, *Int. J. Solids Struct.*, 2003, **40**, 1465-1487.

46 R. E. Robertson, *J. Chem. Phys.*, 1966, **44**, 3950-3956.

47 M. Goldstein, *J. Chem. Phys.*, 1976, **64**, 4767-4774.

48 H. L. Smith, C. W. Li, A. Hoff, G. R. Garrett, D. S. Kim, F. C. Yang, M. S. Lucas, T. Swan-Wood, J. Y. Y. Lin, M. B. Stone, D. L. Abernathy, M. D. Demetriou and B. Fultz, *Nat. Phys.*, 2017, **13**, 900-905.

49 L.-M. Martinez and C. Angell, *Nature*, 2001, **410**, 663-667.

50 L. Zhou, T.-T. Zuo, C. Y. Kwok, S. Y. Kim, A. Assoud, Q. Zhang, J. Janek and L. F. Nazar, *Nat. Energy*, 2022, **7**, 83-93.

51 M. J. Counihan, D. J. Powers, P. Barai, S. Hu, T. Zagorac, Y. Zhou, J. Lee, J. G. Connell, K. S. Chavan and I. S. Gilmore, *ACS Appl. Mater. Interfaces*, 2023, **15**, 26047-26059.

52 D. W. Shin, M. D. Guiver and Y. M. Lee, *Chem. Rev.*, 2017, **117**, 4759-4805.

53 H. T. Takeshita, Y. Kamada, A. Taniguchi, T. Kiyobayashi, K. Ichii and T. Oishi, *Mater. Trans.*, 2006, **47**, 405-408.

54 M. A. Kraft, S. P. Culver, M. Calderon, F. Böcher, T. Krauskopf, A. Senyshyn, C. Dietrich, A. Zevalkink, J. r. Janek and W. G. Zeier, *J. Am. Chem. Soc.*, 2017, **139**, 10909-10918.

55 Y. Tanaka, K. Ueno, K. Mizuno, K. Takeuchi, T. Asano and A. Sakai, *Angew. Chem.*, 2023, **135**, e202217581.

56 B. Singh, Y. Wang, J. Liu, J. D. Bazak, A. Shyamsunder and L. F. Nazar, *J. Am. Chem. Soc.*, 2024, **146**, 17158–17169.

57 A. D. Sendek, E. D. Cubuk, E. R. Antoniuk, G. Cheon, Y. Cui and E. J. Reed, *Chem. Mater.*, 2018, **31**, 342-352.

58 K. T. Butler, F. Oviedo and P. Canepa, *Machine learning in materials science*, American Chemical Society, 2022.

59 B. H. Toby and R. B. Von Dreele, *J. Appl. Crystallogr.*, 2013, **46**, 544-549.

60 C. Farrow, P. Juhas, J. Liu, D. Bryndin, E. Božin, J. Bloch, T. Proffen and S. Billinge, *Journal of Physics: Condens. Matter*, 2007, **19**, 335219.

61 Gaussian 16, Revision C.01, M. J. Frisch, G. W. Trucks, H. B. Schlegel, G. E. Scuseria, M. A. Robb, J. R. Cheeseman, G. Scalmani, V. Barone, G. A. Petersson, H. Nakatsuji, X. Li, M. Caricato, A. V. Marenich, J. Bloino, B. G. Janesko, R. Gomperts, B. Mennucci, H. P. Hratchian, J. V. Ortiz, A. F. Izmaylov, J. L. Sonnenberg, D. Williams-Young, F. Ding, F. Lipparini, F. Egidi, J. Goings, B. Peng, A. Petrone, T. Henderson, D. Ranasinghe, V. G. Zakrzewski, J. Gao, N. Rega, G. Zheng, W. Liang, M. Hada, M. Ehara, K. Toyota, R. Fukuda, J. Hasegawa, M. Ishida, T. Nakajima, Y. Honda, O. Kitao, H. Nakai, T. Vreven, K. Throssell, J. A. Montgomery, Jr., J. E. Peralta, F. Ogliaro, M. J. Bearpark, J. J. Heyd, E. N. Brothers, K. N. Kudin, V. N. Staroverov, T. A. Keith, R. Kobayashi, J. Normand, K. Raghavachari, A. P. Rendell, J. C. Burant, S. S. Iyengar, J. Tomasi, M. Cossi, J. M. Millam, M. Klene, C. Adamo, R. Cammi, J. W. Ochterski, R. L. Martin, K. Morokuma, O. Farkas, J. B. Foresman, and D. J. Fox, Gaussian, Inc., Wallingford CT, 2016.

62 G. Kresse and J. Furthmüller, *Comput. Mater. Sci.*, 1996, **6**, 15-50.

63 G. Kresse and J. Furthmüller, *Phys. Rev. B*, 1996, **54**, 11169.

64 J. P. Perdew, K. Burke and M. Ernzerhof, *Phys. Rev. Lett.*, 1996, **77**, 3865.

65 S. Nosé, *J. Chem. Phys.*, 1984, **81**, 511-519.

66 S. P. Ong, W. D. Richards, A. Jain, G. Hautier, M. Kocher, S. Cholia, D. Gunter, V. L. Chevrier, K. A. Persson and G. Ceder, *Comput. Mater. Sci.*, 2013, **68**, 314-319.

67 Z. Deng, Z. Zhu, I.-H. Chu and S. P. Ong, *Chem. Mater.*, 2017, **29**, 281-288.

68 B. J. Morgan, *Chem. Mater.*, 2021, **33**, 2004-2018.

69 H. Wang, L. Zhang, J. Han and W. E, *Comput. Phys. Commun.*, 2018, **228**, 178-184.

70 A. P. Thompson, H. M. Aktulga, R. Berger, D. S. Bolintineanu, W. M. Brown, P. S. Crozier, P. J. In't Veld, A. Kohlmeyer, S. G. Moore and T. D. Nguyen, *Comput. Phys. Commun.*, 2022, **271**, 108171.